

MARTIN HAMMERSCHMIDT, SVEN HERRMANN, JAN POMPLUN, LIN  
ZSCHIEDRICH, SVEN BURGER, FRANK SCHMIDT

## **Reduced basis method for Maxwell's equations with resonance phenomena**

This paper is made available as an electronic preprint with permission of SPIE and will be published in Proc. SPIE 9630 (2015). The full citation reads:  
*Martin Hammerschmidt, Sven Herrmann, Jan Pomplun, Lin Zschiedrich, Sven Burger and Frank Schmidt, "Reduced basis method for Maxwell's equations with resonance phenomena", Optical Systems Design 2015: Computational Optics, Daniel G. Smith, Frank Wyrowski, Andreas Erdmann, Proc. SPIE 9630 (2015).*  
Copyright 2015 Society of Photo Optical Instrumentation Engineers. One print or electronic copy may be made for personal use only. Systematic electronic or print reproduction and distribution, duplication of any material in this paper for a fee or for commercial purposes, or modification of the content of the paper are prohibited.

Herausgegeben vom  
Konrad-Zuse-Zentrum für Informationstechnik Berlin  
Takustraße 7  
D-14195 Berlin-Dahlem

Telefon: 030-84185-0  
Telefax: 030-84185-125

e-mail: [bibliothek@zib.de](mailto:bibliothek@zib.de)  
URL: <http://www.zib.de>

ZIB-Report (Print) ISSN 1438-0064  
ZIB-Report (Internet) ISSN 2192-7782

# Reduced basis method for Maxwell's equations with resonance phenomena

Martin Hammerschmidt<sup>a</sup>, Sven Herrmann<sup>a</sup>, Jan Pomplun<sup>a,b</sup>,  
Lin Zschiedrich<sup>a,b</sup>, Sven Burger<sup>a,b</sup>, Frank Schmidt<sup>a,b</sup>

<sup>a</sup>Zuse Institute Berlin, Takustraße 7, 14195 Berlin, Germany

<sup>b</sup>JCMwave GmbH, Bolivarallee 22, 14050 Berlin, Germany

This paper is made available as an electronic preprint with permission of SPIE and will be published in Proc. SPIE 9630 (2015). The full citation reads:

*Martin Hammerschmidt, Sven Herrmann, Jan Pomplun, Lin Zschiedrich, Sven Burger and Frank Schmidt, "Reduced basis method for Maxwell's equations with resonance phenomena", Optical Systems Design 2015: Computational Optics, Daniel G. Smith, Frank Wyrowski, Andreas Erdmann, Proc. SPIE 9630 (2015).*

Copyright 2015 Society of Photo Optical Instrumentation Engineers. One print or electronic copy may be made for personal use only. Systematic electronic or print reproduction and distribution, duplication of any material in this paper for a fee or for commercial purposes, or modification of the content of the paper are prohibited.

## ABSTRACT

Rigorous optical simulations of 3-dimensional nano-photonic structures are an important tool in the analysis and optimization of scattering properties of nano-photonic devices or parameter reconstruction. To construct geometrically accurate models of complex structured nano-photonic devices the finite element method (FEM) is ideally suited due to its flexibility in the geometrical modeling and superior convergence properties. Reduced order models such as the reduced basis method (RBM) allow to construct self-adaptive, error-controlled, very low dimensional approximations for input-output relationships which can be evaluated orders of magnitude faster than the full model. This is advantageous in applications requiring the solution of Maxwell's equations for multiple parameters or a single parameter but in real time. We present a reduced basis method for 3D Maxwell's equations based on the finite element method which allows variations of geometric as well as material and frequency parameters. We demonstrate accuracy and efficiency of the method for a light scattering problem exhibiting a resonance in the electric field.

**Keywords:** finite element method, rigorous optical modeling, photonic crystals, reduced basis method, reduced order models, electromagnetic field solver

## 1. INTRODUCTION AND PROBLEM SETTING

Optical simulations of nano-photonic structures with complex geometries are important in the analysis of their scattering properties. In applications ranging from optimization of structures to scatter or absorb light efficiently to reconstruction of geometrical features from measurements high accuracy solutions of Maxwell's equations are used. The finite element method is ideally suited to construct geometrically accurate models of complex structured nano-photonic devices and to compute high accuracy solutions of the time-harmonic vectorial Maxwell's equations in 3D.<sup>1</sup> It can outperform other rigorous electromagnetic field solvers if the accuracy demands are high.<sup>2</sup> However, for some applications like optical critical dimension metrology, the solution of Maxwell's equations is required for multiple parameters or in real time.<sup>3</sup> Reduced order models such as the reduced basis method (RBM) allow to construct self-adaptive, error-controlled, very low dimensional approximations for input-output relationships which can be evaluated orders of magnitude faster than the full model.<sup>4-7</sup>

In the following, we investigate a self-adaptive, error-controlled reduced basis method<sup>6</sup> based on the finite element solver JCMSuite<sup>8</sup> suited for the construction of reduced order models for nonlinear output functionals

---

Further author information: (Send correspondence to Martin Hammerschmidt)

Martin Hammerschmidt: E-mail: hammerschmidt@zib.de, Telephone: +49 30 84185-149

and parameter dependencies. The underlying finite element solver has been previously applied to a variety of applications in different fields.<sup>9–14</sup> Here we discuss a reduced order model for a two-dimensional array of nano-holes exhibiting photonic bands. This structure has been investigated before both experimentally and numerically.<sup>15</sup> We revisit the problem using a reduced basis for the illumination parameter (wavelength and angle of incidence). We perform a convergence analysis and demonstrate accuracy of the obtained results.

We demonstrate the accuracies that can be reached by the reduced model for the illumination parameters in case of a high-quality resonance in the electric field.

This paper is structured as follows: The background of the numerical methods is presented in Sections 2 and 3. The reduced basis method is applied to an example exhibiting resonances in Section 4. Details of the photonic crystal example are presented first, followed by a detailed discussion of the reduced basis construction, the online evaluation and the various error sources in the approximation.

## 2. FINITE ELEMENT METHOD

In the following we briefly summarize the main idea of the finite element method (FEM).<sup>1,16</sup> This section serves as a motivation for the reduced basis method presented hereafter. Light scattering off nano-structures with a monochromatic light source in frequency domain is governed by the linear Maxwell's equation. These can be reformulated to form the following, single second order curl-curl equation for the electric field  $\mathbf{E}$

$$\nabla \times \mu^{-1} \nabla \times \mathbf{E} - \omega^2 \varepsilon \mathbf{E} = i\omega \mathbf{j}. \quad (1)$$

with the permeability and permittivity tensors  $\mu$  and  $\varepsilon$ .  $\omega$  is the frequency of the time-harmonic field and the electric current density  $\mathbf{j}$  models electromagnetic sources within the computational domain  $\Omega$ . The exterior  $\Omega_{ext} = \mathbb{R}^3 \setminus \Omega$  is infinite and hosts incoming electric fields which act as sources in the interior  $\Omega$ . A transparent boundary condition has to be applied at the boundary  $\Gamma$ . The perfectly matched layer method (PML) is used in our solver.

The finite element discretization is based on the variational formulation of (1). This is derived by multiplication with a vector valued test function  $\varphi$  and subsequent integration over  $\mathbb{R}^3$  resulting in

$$\int_{\mathbb{R}^3} \nabla \times \varphi \mu^{-1} \nabla \times \mathbf{E} - \omega^2 \varphi \varepsilon \mathbf{E} = i\omega \int_{\mathbb{R}^3} \varphi \mathbf{j} \quad (2)$$

which is abbreviated in the following as  $a(\varphi, \mathbf{E})$  with the right hand side  $f(\varphi)$ .

As the choice of  $\varphi$  is arbitrary we demand (2) to hold for any  $\varphi$  and choose  $H(\mathbf{curl}, \Omega)$  as the proper function space for  $\mathbf{E}$  and  $\varphi$ . The weak formulation of (1) now reads: Find  $\mathbf{E} \in H(\mathbf{curl}, \Omega)$  such that:

$$a(\varphi, \mathbf{E}) = f(\varphi) \quad \forall \varphi \in H(\mathbf{curl}, \Omega). \quad (3)$$

The space  $H(\mathbf{curl}, \Omega)$  is infinite. For a numerical solution of (3) we restrict the solution space to a finite dimensional subspace  $V_h \subset H(\mathbf{curl}, \Omega)$  with  $\dim V_h = N < \infty$ . It is sufficient to demand (3) to hold for a basis  $\{\varphi_1, \dots, \varphi_N\}$  of  $V_h$ . Every element  $\mathbf{E} = \sum_{i=1}^N \alpha_i \varphi_i$  of  $V_h$  can be expanded in this basis. Hence (3) in  $V_h$  is equivalent to the linear system

$$\sum_{i=1}^N a(\varphi_j, \varphi_i) \alpha_i = f(\varphi_j) \quad j = 1, \dots, N \quad (4)$$

The choice of  $V_h$  determines the structure of the matrix  $A = (a(\varphi_j, \varphi_i))_{i,j=1}^N$ . Ideally, this matrix is sparse allowing to compute the coefficients  $\alpha_i$  with an efficient LU decomposition.

The choice of basis functions of  $V_h$  determines the structure of  $A$ . Basis or ansatz functions with only a local support yields the desired sparsity of  $A$ . The idea of a finite element discretization is to decompose the computational domain  $\Omega$  into simple geometrical patches or elements such as tetrahedrons, prisms or bricks. To this resulting spatial discretization called mesh we associate a positive scalar  $h$  describing the spatial resolution of the patches. The ansatz functions are then chosen as polynomials of order  $p$  or less over the patches. The

order  $p$  does not have to be chosen identical on all patches or in all spatial directions of a patch but can be adapted to the chosen spatial resolution. It can be lowered in regions where the spatial resolution is high and increased where it is low.

This yields the  $hp$  finite element method<sup>17</sup> which yields very accurate results of (3). By increasing the mesh density  $h$  or the polynomial order  $p$  the total number of unknowns  $\mathcal{N}$  is increased resulting in a more accurate solution but at the same time the numerical complexity to solve the linear system (4) is increased as well. A problem adapted balancing of  $h$  and  $p$  yields usually the best results in terms of computational complexity.

### 3. REDUCED BASIS METHOD

The reduced basis method (RBM)<sup>4-6,18</sup> is one of the most widely used model order reduction methods.<sup>3,19</sup> It offers a way to construct error controlled approximations to input-output relationships. Here, input refers to a specific configuration of parameters  $\mu \in \mathbb{R}^d$  whereas the output usually refers to an output quantity  $s(\mu) = s(\mathbf{E}(\mu))$  derived from a solution  $\mathbf{E}$  of a parameter dependent partial differential equation. The RBM and FEM exhibit many similarities such as the Galerkin projection. Whereas the finite element solution is based on polynomial ansatz functions with local support, the reduced basis solution is a superposition of globally defined fields. The resulting linear system is thus small and dense instead of the high-dimensional, sparse system we obtain for the finite element discretization.

We consider parameterized electromagnetic scattering problems where the parameter  $\mu$  may describe geometry and material variations or properties of the illumination. For any given parameter we may solve (3) with a finite element discretization with  $\mathcal{N}$  degrees of freedom and compute the output of interests e.g. the Fourier transform of the electric field or the electric field energy contained within a subdomain of  $\Omega$ . We refer to such a solution as a *truth solution*. The computation of truth solutions  $\{\mathbf{E}(\mu) | \mu = \mu_1, \mu_2 \dots\}$  becomes quickly infeasible if the number of parameter configurations considered is large. The purpose of the reduced basis approximation

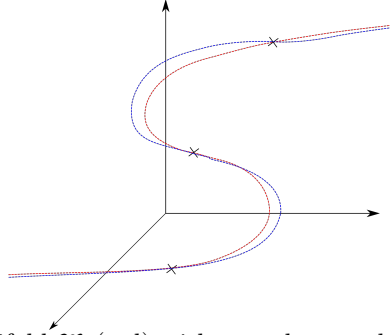


Figure 1: Solution manifold  $\mathfrak{M}$  (red) with snapshots and RB approximation (blue)

is to provide a low-dimensional approximation to the high dimensional problem (3) for all parameters  $\mu \in \mathfrak{D}$ . We assume the manifold of all solutions  $\mathfrak{M} = \{\mathbf{E}(\mu) \text{ is a solution to (3)} \mid \mu \in \mathfrak{D}\}$  to be approximated by a low dimensional subspace  $X_N$  of dimension  $N$ . A schematic of the solution manifold (red) is depicted in Figure 1 together with an approximation (blue) using three snapshots indicated as crosses. The idea of this method is now closely related to the finite element method presented in the previous section. Instead of searching the solution to the parameter dependent PDE in the high dimensional finite element space  $V_h$  (where oftentimes  $\mathcal{N} > 10^6$ ) we restrict the space to a very low dimensional (usually of dimension  $N = O(10)$ ) *reduced basis space*  $X_N$ , i.e. we solve the reduced problem:

For  $\mu \in \mathfrak{D}$  find  $\mathbf{E}_N \in X_N$  such that:

$$a(\varphi, \mathbf{E}_N; \mu) = f(\varphi; \mu) \quad \forall \varphi \in X_N. \quad (5)$$

The obvious choice is to choose  $N$  linearly independent truth solutions to span  $X_N$ . We call these *snapshots* and  $\Phi = \{\phi_i\}_{i=1}^N$  where  $\text{span} \Phi = \text{span}\{\mathbf{E}(\mu_i) \mid \mathbf{E}(\mu_i) \text{ is a truth solution for } \mu_i, i = 1, \dots, N\}$  a *reduced basis*.

### 3.1 Offline-online decomposition

Key in the efficient computation is an online-offline decomposition where all numerical operations involving the number of degrees of freedom  $\mathcal{N}$  of the underlying finite element solution are executed in the offline phase. In the subsequent online phase during the actual application only a very low dimensional system has to be assembled and solved for every parameter configuration. The solution  $\mathbf{E}(\mu) = \sum_{i=1}^N \alpha_i \phi_i$  can be expanded in the reduced basis  $\Phi$  and entered into (5). The resulting linear system

$$\sum_{i=1}^N \alpha_i a(\phi_j, \phi_i; \mu) = f(\phi_j; \mu) \quad j = 1, \dots, N \quad (6)$$

is of dimension  $N$  but depends on  $\mu$ . If the sesquilinear form  $a(\cdot, \cdot)$  and the linear form  $f(\cdot)$  are affine in the parameter, i.e.  $a(\phi, \xi; \mu) = \sum_{q=1}^Q \theta_q(\mu) a_q(\phi, \xi)$  and  $f(\phi; \mu) = \sum_{q=1}^Q \theta_q(\mu) f_q(\phi)$ , assembly and solution of (6) only depends on  $N$  and  $Q$  but not on  $\mathcal{N}$ . The  $\mathcal{N}$ -dependent matrices  $(A^q)_{i,j} = a_q(\phi_i, \phi_j)$  and vectors  $(f^q)_i = f_q(\phi_i)$  can be precomputed. Most parameterizations of the electromagnetic scattering problem do not exhibit an affine expansion in the parameter. For these situations the empirical interpolation method was developed<sup>20,21</sup> and successfully applied to a number of applications.<sup>22,23</sup>

We call the construction phase in which  $N$  truth solutions are computed to span  $X_N$  and the matrices  $A^q$  and vectors  $f^q$  are computed the *offline* phase. The  $\mathcal{N}$ -independent second step of assembling and solving (6) for a given  $\mu$  is called the *online* phase. Similar to the reduced matrices  $A^q$  a linear or quadratic output of interest can be projected onto  $X_N$  to achieve an evaluation of the reduced quantity  $s(\mathbf{E}_N(\mu))$  independent of  $\mathcal{N}$ .

### 3.2 Basis construction

The choice of  $X_N$  influences the quality of the reduced approximation. Ideally we want to choose  $X_N$  optimally. In general this is not possible a priori. Building  $X_N$  self-adaptively from optimally placed snapshots and estimating and controlling the approximation error over  $\mathfrak{D}$  yields a sequence of reduced basis spaces  $X_N$  which contains the maximal available information about  $\mathfrak{M}$  for any  $N$ . The optimization problem for the snapshot placement is solved with a so-called *Greedy* selection of the worst resolved parameter location within a finite dimensional training set  $\mathfrak{D}_{train} \subset \mathfrak{D}$ . This requires rigorous a posteriori error estimators to assess the approximation error. These are available for the electromagnetic scattering problem and usually based on the dual norm of the residuum.<sup>6,18</sup>

## 4. REDUCED BASIS METHOD FOR PROBLEMS WITH RESONANCE PHENOMENA

The reduced basis method relies on the assumption that the solution manifold can be approximated well by snapshot solutions. In case of a structure exhibiting resonant behaviour the field solution changes drastically with small variations of a parameter. In the following we build a reduced basis for such a model and present the reduced model as well as the limits of the method for this example.

### 4.1 Optical model of a 2D photonic crystal made of silicon

Photonic crystals are periodic structures that inhibit propagation of electromagnetic waves of frequencies within a specific frequency band called photonic band gap. Repeating material patterns are introduced through (nano-) structuring of materials for example in gratings.<sup>24</sup> Hexagonal arrays of holes in a high-index material are among the most frequently investigated structures. They give rise to pronounced photonic band gaps and are envisioned to be used in a variety of applications such as solar cell light management or upconversion as well as optical sensing.

In a previous study we investigated the absorption properties and the excitation of high-intensity near-fields within periodic, conical *nanoholes* of a silicon slab.<sup>15</sup> The optical model presented here is identical to our previous investigations.<sup>15</sup> The unit cell of the structure is shown in Figure 2 in real space, in k-space and as volume meshes. The cell has a pitch of 600 nm and the conical hole has a sidewall angle of 17°. The diameter of the hole is 385 nm at the centre of the 390 nm thick slab. The unit cell is split into four subdomains: the

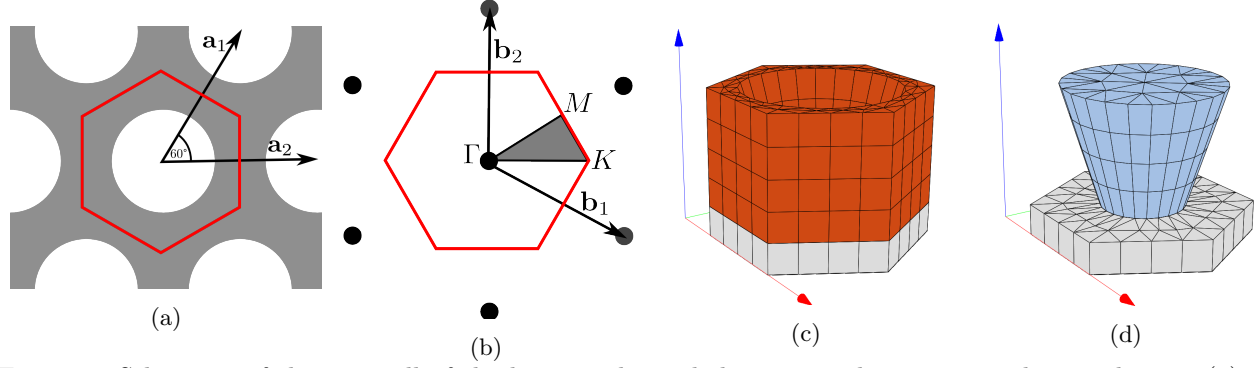


Figure 2: Schematic of the unit cell of the hexagonal nanohole array with 600 nm pitch in real space (a) and k-space (b). The high-symmetry points of the irreducible Brillouin zone (grey) are marked. (b) The silicon slab (orange) sits on a glass substrate (gray) and is 390 nm thick. (c) The conical hole (blue) is centered in the unit cell with a sidewall angle of  $17^\circ$  and has a diameter of 385 nm at the center of the slab. An air layer (100 nm thick, not shown) completes the cell. In  $\pm z$  directions transparent boundary conditions are applied.

silicon slab, the hole, the glass substrate and the air layer of 100 nm thickness above the array. In  $\pm z$  directions transparent boundary conditions are applied, i.e. the air and glass domains are extended via PML-layers. The p-polarized illumination from the upper half-space is varied in wavelength  $\lambda$  and incidence angle  $\theta$  along the  $\Gamma$ -K-direction. The refractive index of silicon<sup>25</sup> is dispersive but real-valued in the investigated wavelength range and  $n_{air} = 1$ ,  $n_{glass} = 1.53$  are kept constant. The FEM discretization with fourth-order elements and accurate PML-settings yields a system with  $\mathcal{N} = 249\,540$  unknowns.

Previously we computed near-field enhancements as an increased electromagnetic field energy density in and 100nm above the hole normalized by the same quantity for the incident field in free space. The resonance bands depicted in Figure 3 for p-polarized illumination from the upper half-space tilted along the  $\Gamma - K$  direction were also observed in experimental reflection measurements and good agreement between experimental and numerical results was found.<sup>15</sup> The photonic crystal exhibits several distinct resonances corresponding to resonance modes of the photonic crystal with high quality factors in both polarizations which strongly depend on the wavelength and incidence angle of the illumination.

## 4.2 Reduced basis construction

We construct a reduced basis for the illumination parameters  $\lambda$  and  $\theta$  in the parameter domain  $\mathfrak{D} = [1200 \text{ nm}, 1280 \text{ nm}] \times [14^\circ, 20^\circ]$ . The reduced model is built for the electric field energy density integration to compute field enhancements in the four subdomains of the array. Note that this is a quadratic output quantity and we will often shorten it to *density integration*.

The training set  $\mathfrak{D}_{train}$  used for the various Greedy searches is chosen to be quite dense to adequately resolve all features within  $\mathfrak{D}$ . It initially comprises  $101 \times 21$  sampling points in an equidistant grid along  $\lambda$  and  $\theta$  axis.

The EIM approximation is executed using a tolerance of  $\epsilon_{EIM} = 1 \cdot 10^{-7}$ . For the empirical interpolation of the system matrix  $Q_A = 3$  snapshots are required leading to an estimated error of  $\delta_{EIM}^A = 7.45 \cdot 10^{-12}$  over the training set  $\mathfrak{D}_{train}$ . Using the same training set, we find requirements of  $Q_b = 8$  and  $Q_{PP} = 2$  for the empirical interpolation of the source terms and the quadratic post processes. The resulting approximation errors over  $\mathfrak{D}_{train}$  are  $\delta_{EIM}^b = 9.42 \cdot 10^{-8}$  and  $\delta_{EIM} = 7.24 \cdot 10^{-13}$  respectively.

In the offline phase 30 snapshots are computed to build the reduced basis for the parameter space  $\mathfrak{D} = [1200 \text{ nm}, 1280 \text{ nm}] \times [14^\circ, 20^\circ]$ . Figure 4b depicts the location of the chosen snapshots (crosses) in the parameter domain. The colour coding indicates the sequence in which the snapshots were chosen (dark to light markers). The first snapshot is chosen in the center of the parameter domain and the subsequent snapshots are determined by the Greedy algorithm. The choice of snapshot locations follows the boundaries of  $\mathfrak{D}$ . This is in line with other publications where similar observations were made.<sup>7</sup> The first selected snapshots cover the extreme positions

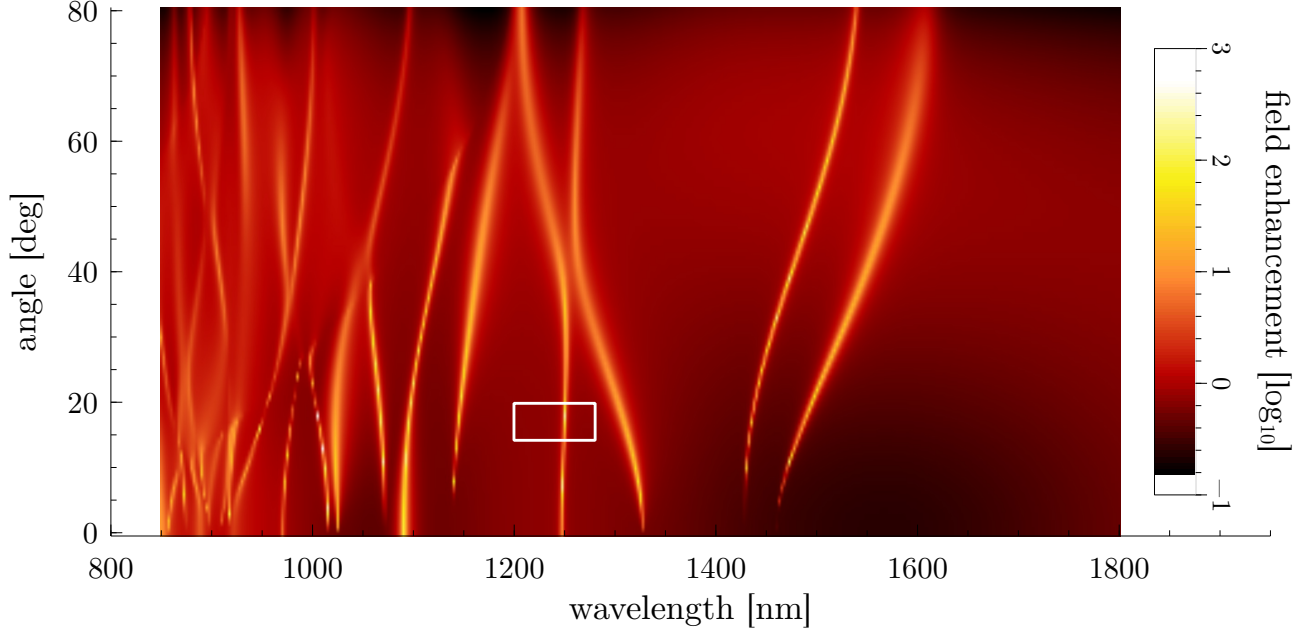


Figure 3: Simulated field enhancement pattern of the nanohole array on logarithmic scale. The field enhancement is measured in the hole and 100 nm above the array and normalized with the field energy of a plane wave in the respective volume. The incident wave is p-polarized and tilted along the  $\Gamma - K$  direction. The white line marks the cut shown in b). The rectangle marks the limits of the parameter domain of the reduced order model discussed in this section.

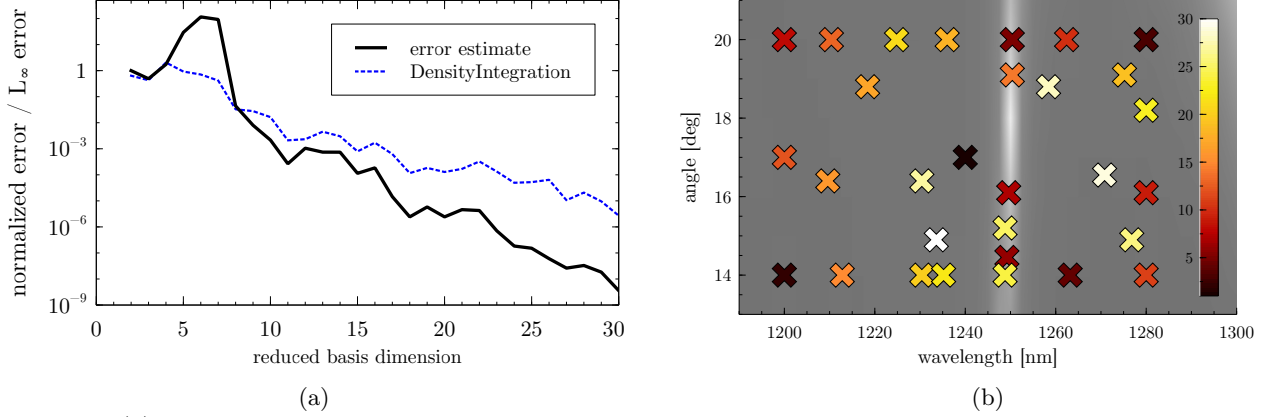


Figure 4: (a): Error estimates with increasing reduced basis dimension in a semi-logarithmic plot. The residual error estimate (black line) is normalized with the estimate for  $N = 1$ . The error estimate for the DensityIntegration (blue line) uses the  $L_\infty$ -norm. (b): Snapshot positions in parameter space are marked as crosses. They are superimposed on a gray-scale logarithmic plot of the field enhancement. The colour of the marker indicates the sequence of snapshot selection from darker to lighter colours. The first snapshot chosen is the center of the parameter domain. Most snapshots are located at the boundaries of the parameter domain. A cluster of snapshots lies along the resonance band at approximately 1250 nm.



(1200, 14) and (1280, 20). Along the resonance band we find 6 snapshots in total with the first 3 snapshots chosen in iterations 5-7.

The reduced basis offline phase choses the snapshots according to a Greedy strategy depending on the error estimate for the worst-resolved parameter in the training set. Hence the estimated error generally decreases with increasing Greedy iterations. In Figure 4a the error estimates with increasing reduced basis dimension is shown in a semi-logarithmic plot. The black line shows the normalized residual error estimate for increasing reduced basis dimension  $N$ . The maximum of the error estimate in the first Greedy iteration is used as a normalization factor. The error first increases to a maximum of  $1 \cdot 10^2$  at  $N = 6$  before dropping to a level of  $1 \times 10^{-2}$  at  $N = 8$ . Subsequently we observe exponential convergence of this error estimate up to a level of  $3.59 \cdot 10^{-9}$ . The increase is caused by the resonance band traversing the parameter domain at  $\approx 1250$  nm. As this area is poorly approximated by the first snapshots, the error estimate increases momentarily, leading to the maximum in Figure 4a. The dashed blue graph for the *DensityIntegration* depict the estimated error in the  $L_\infty$ -norm. The graph exhibits an exponential reduction of the error over the training set up to approximately  $2 \cdot 10^{-6}$ .

### 4.3 Online evaluation of the reduced basis

In the online phase the reduced basis allows to evaluate the reduced order models in milliseconds instead of around 4 minutes a truth solution with FEM requires. Due to limited computational capacities, the field pattern in Figure 3 is computed on a coarse, equidistant cartesian grid with  $381 \times 81$  points. Within the parameter domain of interest  $\mathfrak{D}$  lie only  $33 \times 7$  values. As the resonance width of 1.5 nm is close to the distance between two grid points it is unlikely to judge its maximum enhancement correctly.

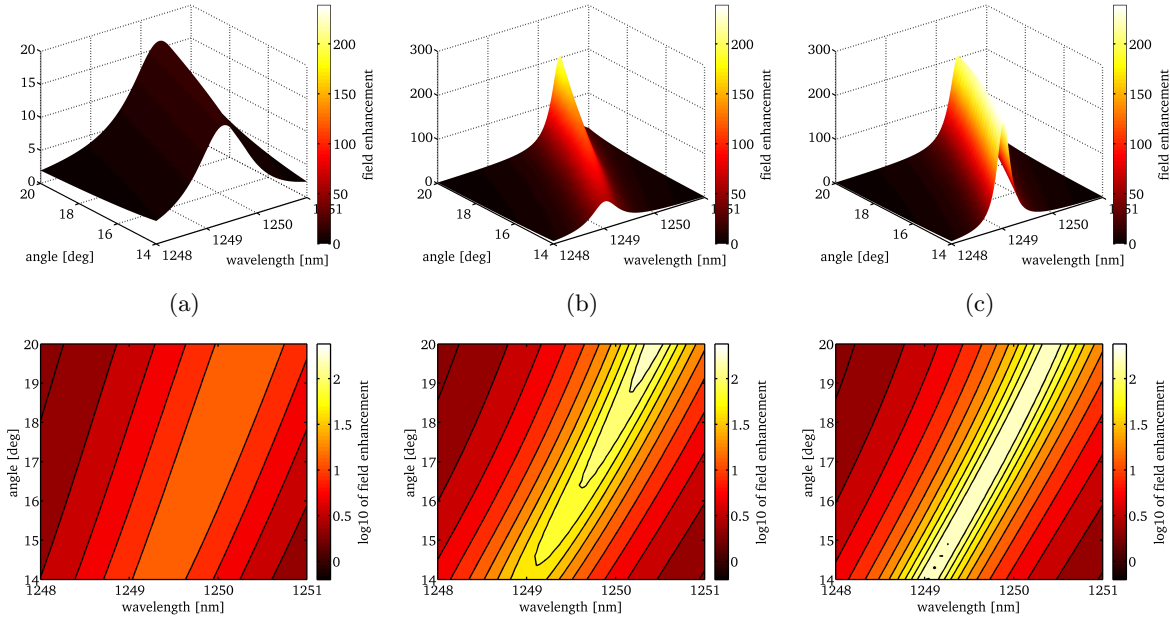


Figure 5: Field enhancements computed by evaluation of the Reduced Basis in the vicinity of the resonance wavelength as surface plots (top row) and logarithmically scaled contour plots (bottom row). The columns correspond to using 4 snapshots (a), 5 snapshots (b) and 11 snapshots (c).

The reduced basis allows to evaluate the field enhancement over  $\mathfrak{D}$  much faster and with increased resolution in parameter space. We focus the evaluation to the vicinity of the resonance band between 1248 nm and 1251 nm and use  $101 \times 21$  sampling points arranged in an equidistant grid. The evaluation of the reduced basis with the full dimension takes 205.62 s for the sampling set of 2021 evaluation points. The majority of the time is spent generating the input for the solver in MATLAB (105 s). Subsequently, each evaluation takes on average 358.4 ms on a single core for the full reduced basis dimension. This includes inversion of the reduced system, the post processing and writing of output files. The speed up factor compared to the truth approximation is about 2300 for this example.

In Figure 5 the results of three evaluations using different numbers of snapshots are shown as surface plots on the top and as contour plots with logarithmic scaling on the bottom. In the first column (a) the reduced basis is evaluated using 4 snapshots. The field enhancement pattern is poorly recovered as none of the employed snapshot lies on or near the resonance band (cf. discussion of recognition of the resonance in the error estimate above and Figure 4b). The error contour indicates large deviations along the resonance band. As the fifth selected snapshot lies on the resonance band, the field enhancement with 5 snapshots in the second column (b) is much better. The error contour still indicates deviations along the band. The resonance is correctly approximated in the third column (c) with 11 snapshots.

#### 4.4 Error analysis

The error of reduced basis approximation can be understood and measured in different ways. In most applications the error in the output quantities is of particular interest but also the error in field solution itself might be of interest. We thus compare the reduced basis approximation and two sets of reference solutions for two randomly chosen parameter ensemble  $\Xi_{1,2} \subset \mathcal{D}_{train}$  of 500 parameters. Figure 8 shows the distribution of the parameter locations in  $\Xi_1$  as crosses. For these parameters  $\mu \in \Xi_1$  we solve the full FEM problem without any approximation. Note that these reference solutions are not solutions of the truth approximation which includes the empirical interpolation approximation of the system matrix and right-hand sides. We compute a second set of reference solutions over the parameter ensemble  $\Xi_2 \subset \mathcal{D}_{train}, \Xi_1 \neq \Xi_2$  as solutions of the truth approximation including the empirical interpolation for the system matrix and right-hand side.

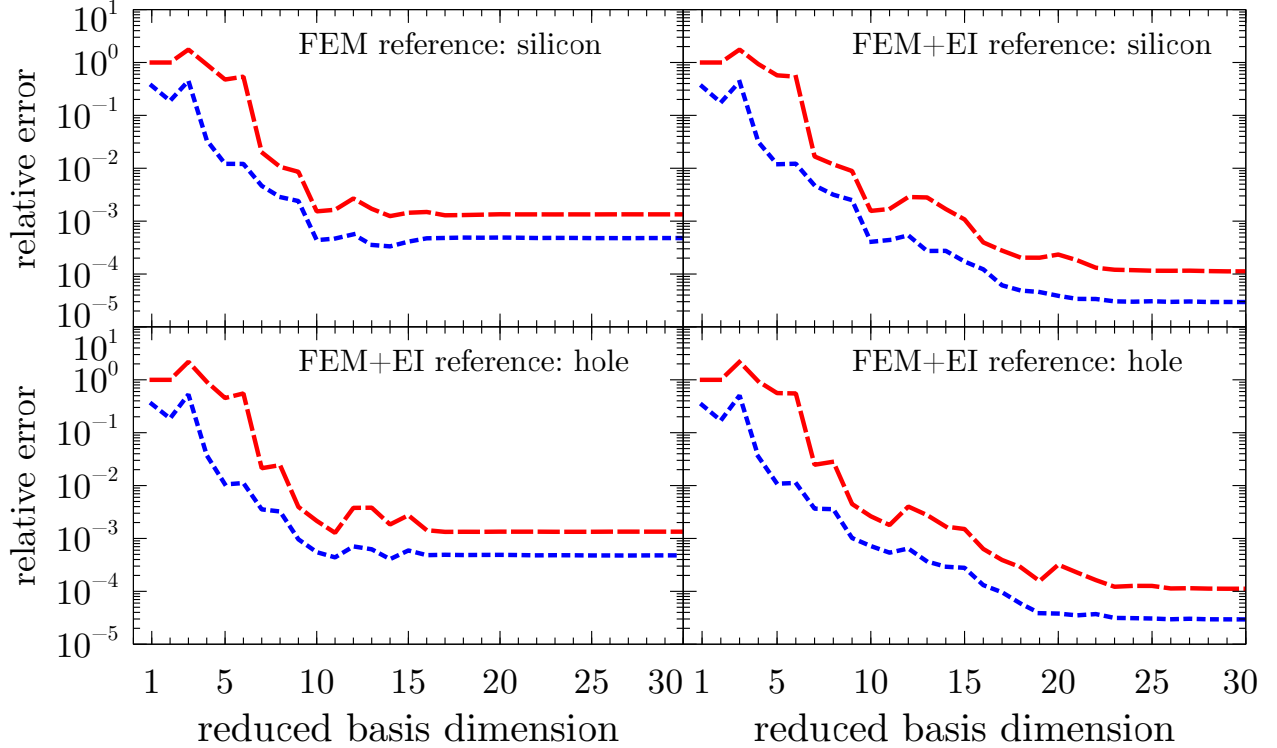


Figure 6: Relative error in the quadratic *density integration* output quantity over the reduced basis dimension measured in the  $L_\infty$  norm. There is one plot per subdomain which is indicated in the upper right corner of each axis. The depicted errors are the maximal error (red dashed line) and the mean error (blue dashed line) over the set  $\Xi_1$ . The reference solutions fulfill the truth approximation without (left column) and with (right column) empirical interpolation.

**Quantity of interest** We compare the output quantity to the reference solutions by measuring the relative errors. In Figure 6 the relative errors over  $\Xi_1$  (left column) and  $\Xi_2$  (right column) are depicted for two quadratic

quantities, the *density integration* of the electric field energy density in the silicon and hole subdomains. Each plot shows the maximum error over  $\Xi_i$  (red) and the mean error (blue). Both quantities exhibit an identical convergence trend as do the omitted quantities of the remaining subdomains.

For the full FEM reference solutions shown in the left column an initial plateau of the error is followed by a steep decrease of the error before a stagnation sets in at  $N = 15$ . The maximum errors saturate at  $1 \cdot 10^{-3}$  with the mean slightly lower. The stagnation is readily explained: The reference solutions used for comparison is not identical to the solution approximated by the reduced basis. The reference solution used for comparison here does not include the empirical interpolation error. Hence we cannot expect convergence of these quantities beyond the accuracy of the solution itself. At the resonances we are close to or at this accuracy limit.

The reference solutions with the empirical interpolation included are the truth solutions approximated by the reduced basis itself. The error in the output quantities for these references are depicted in the right column. We observe a convergence behaviour almost identical to the previous case up to  $N = 10$ . Here, the maximal error decreases even beyond  $N = 15$  and finally saturates at  $1 \cdot 10^{-4}$ . The error mean is almost an order of magnitude smaller. The saturation can be attributed to the empirical interpolation error introduced in the approximation of the quadratic post process and not to the convergence of the field solution itself as in the previous case. This is demonstrated in Figure 7.

**Field solution** The output functionals are continuous functions of the field solution. Hence we do not expect a fundamentally different result in studying the approximation error of the field solution. In Figure 7 the convergence of the mean and maximum of the error in the  $H(\mathbf{curl}, \Omega)$  norm is shown as well as the relation between the reduced basis error estimate and the  $H(\mathbf{curl}, \Omega)$ -error. The mean and maximum of the error over  $\Xi_2$  have identical trends and fit those of the output quantities in Figure 6. The errors initially are constant before dropping 6 orders of magnitude at  $N = 7$ . The errors decrease exponentially beyond  $N = 21$  up to a level of at most  $2.09 \cdot 10^{-8}$  with a mean of  $5.14 \cdot 10^{-10}$ . The drop of the error coincides with the inclusion of snapshots in the resonance band into the reduced basis (compare Figure 4b). Once these have been included in the basis, the errors are orders of magnitude smaller.

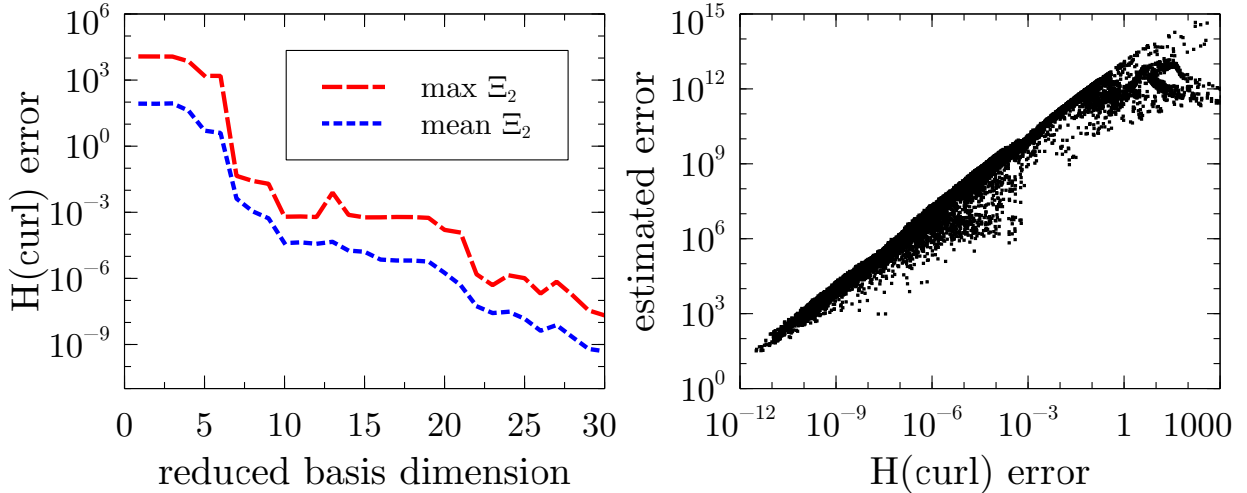


Figure 7: Maximum and mean error of  $\Xi_2 \subset \mathfrak{D}_{train}^N$  in  $H(\mathbf{curl}, \Omega)$  norm over the reduced basis dimension (left) and estimated reduced basis error over the error in  $H(\mathbf{curl}, \Omega)$  norm (right). The maximal and mean error decrease with increased reduced basis dimension. The estimated and actual error are highly correlated.

The scatter plot relating estimated error and  $H(\mathbf{curl}, \Omega)$  error demonstrates the good performance of the error estimate. The correlation coefficient  $\rho > 0.96$  indicates a high correlation. The errors are correctly approximated by the residual error estimate over the complete range of 15 orders of magnitude. The resonance structure of the field solution accounts for the outliers in the bulges of the distribution. Due to the resonance, the  $H(\mathbf{curl}, \Omega)$  norm of the reference solutions differs greatly over the parameter domain. The statistics in Table 1 show this in

Table 1: Statistics of the  $H(\mathbf{curl}, \Omega)$  norm of the reference solutions over  $\Xi_1$

mean	min	max	median	standard deviation
89.28	15.24	8840.50	17.37	525.48

detail. In relation to the norm of the solution, the approximations are orders of magnitude better than indicated by maximum of the absolute error shown here.

**Inf-sup constant estimation** The residual error estimate used here does neither account for the empirical interpolation error nor the inf-sup constant  $\beta$ . As demonstrated, neglecting the empirical interpolation error is problematic at high accuracies. Neglecting the estimation of the inf-sup constant prevents the use of the term *certified* in the context of our reduced basis implementation, but comes at greatly reduced computational costs. In this example the inf-sup-constant varies between 0.18 and 0.50. The distribution of  $\beta$  over  $\mathfrak{D}$  shown in Figure 8 exhibits a band structure where  $\beta$  is constant over large areas. This naturally follows from the frequency selective behaviour of the structure. The histogram in the same Figure shows the clustering around 0.19 and 0.23.

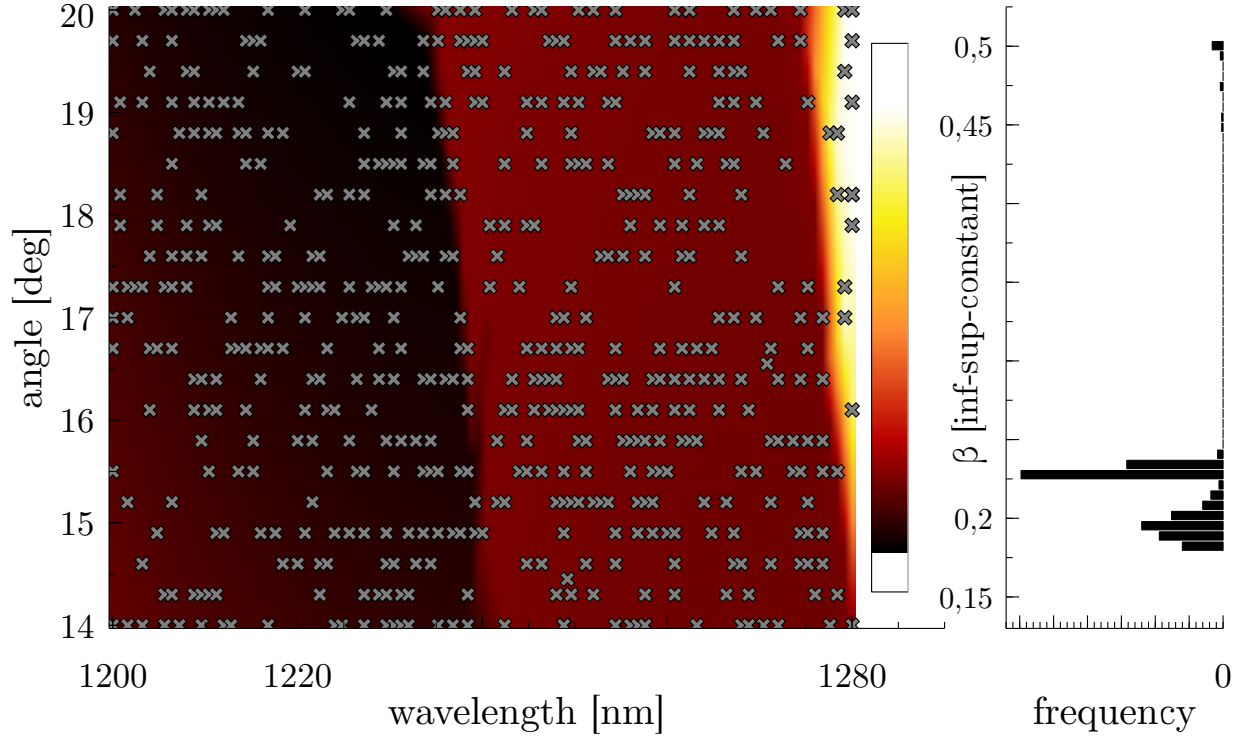
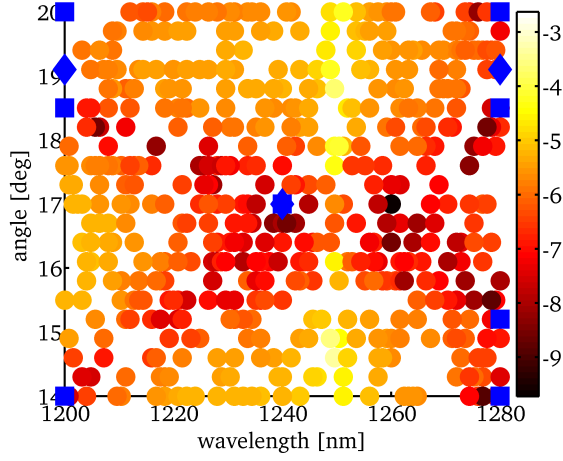
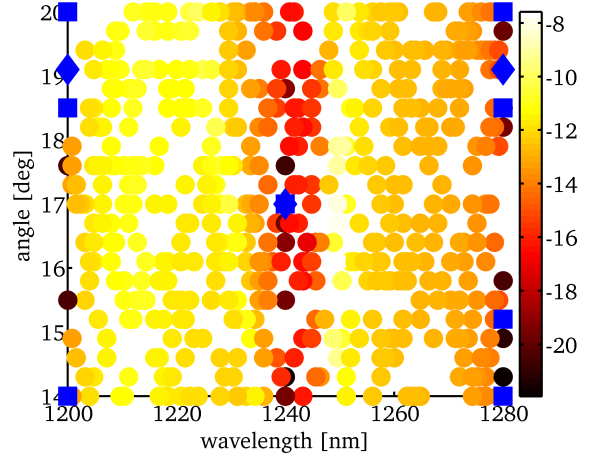


Figure 8: The pseudo colour plot of the inf-sup constant  $\beta$  distribution in parameter space  $\mathfrak{D}$  for 500 randomly selected values (indicated by crosses) of the finest training set  $\mathfrak{D}_{train}^N$ . The colorbar bar axis coincides with the histogram on the right showing the clustering of  $\beta$  for the 500 datapoints.

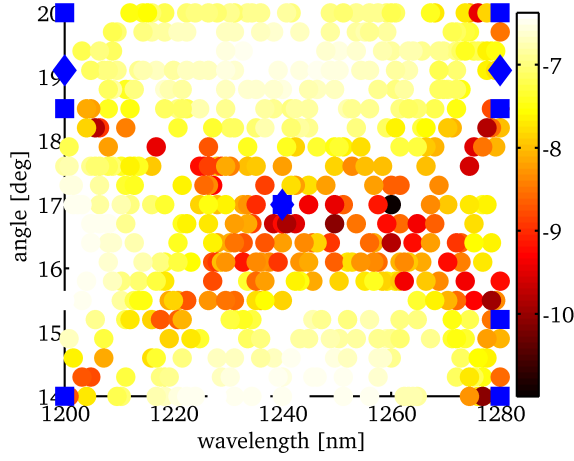
**Empirical interpolation error** The error introduced by the affine expansion of the bilinear form with the empirical interpolation method is measured and controlled in the  $L_\infty$  norm. We investigate two errors related to the empirical interpolation approximation for a set  $\Xi_2 \subset \mathfrak{D}$  of 500 parameters. In the discretized system the



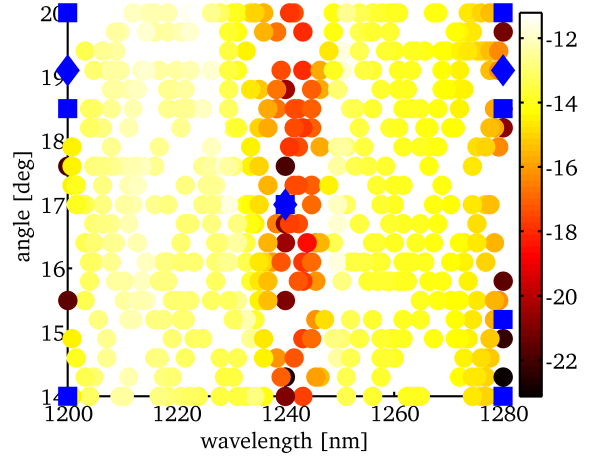
(a) Error  $\Delta_1$  (logarithmic scale)



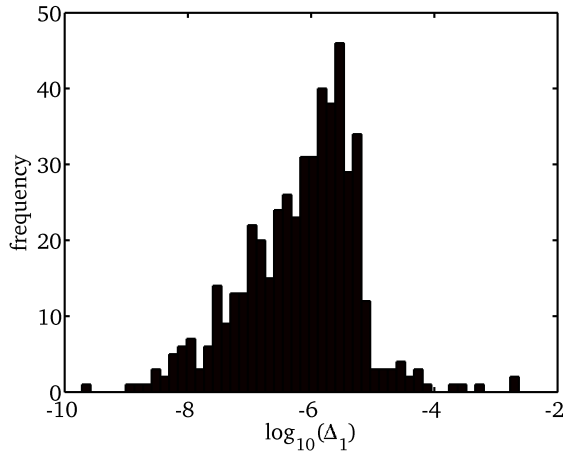
(b) Error  $\Delta_2$  (logarithmic scale)



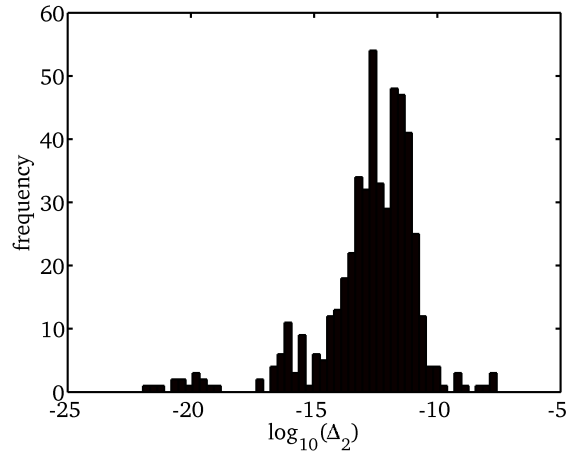
(c) Error  $\delta_1$  (logarithmic scale)



(d) Error  $\delta_2$  (logarithmic scale)



(e) Histogram of  $\log_{10}(\Delta_1)$



(f) Histogram of  $\log_{10}(\Delta_2)$

Figure 9: (a)-(d): Scatter plots of the empirical interpolation error  $\Delta_{1,2}$  (absolute) and  $\delta_{1,2}$  (relative) for the set  $\Xi_2 \subset \mathfrak{D}$  (see text for definitions). The positions of the EIM snapshots for the matrix (diamonds) and right-hand sides (squares) are marked blue. (e)-(f): Histograms of  $\log_{10}(\Delta_1)$  and  $\log_{10}(\Delta_2)$ .

matrix  $\mathcal{A}$  is approximated by  $\mathcal{A}_{eim}$  and the right hand side  $\mathbf{b}$  by  $\mathbf{b}_{eim}$ . We compare the solutions

$$\begin{aligned}\mathbf{x} &= \mathcal{A}^{-1}\mathbf{b}, \\ \mathbf{x}_{eim} &= \mathcal{A}_{eim}^{-1}\mathbf{b}_{eim}, \\ \tilde{\mathbf{x}} &= \mathcal{A}^{-1}\mathbf{b}_{eim}.\end{aligned}$$

This motivates the definition of the following absolute errors

$$\begin{aligned}\Delta_1 &= \|\mathbf{x} - \mathbf{x}_{eim}\|_{\mathbf{H}(\mathbf{curl}, \Omega)}, \\ \Delta_2 &= \|\tilde{\mathbf{x}} - \mathbf{x}_{eim}\|_{\mathbf{H}(\mathbf{curl}, \Omega)}\end{aligned}$$

and similarly relative errors

$$\begin{aligned}\delta_1 &= \frac{\Delta_1}{\|\mathbf{x}_{eim}\|_{\mathbf{H}(\mathbf{curl}, \Omega)}}, \\ \delta_2 &= \frac{\Delta_2}{\|\mathbf{x}_{eim}\|_{\mathbf{H}(\mathbf{curl}, \Omega)}}.\end{aligned}$$

The computed errors over  $\Xi_2$  are shown in Figure 9 on logarithmic scales as scatter plots together with histograms.  $\Delta_1$  (Figure 9a) exhibits its maximal values along the resonance band. We find values larger than  $1 \cdot 10^{-5}$  for  $\Delta_1$  in this region with a maximum of 0.0024. However, the relative error  $\delta_1$  at this parameter location is only  $2.75 \cdot 10^{-7}$ . Similarly, we observe  $\delta_1$  (Figure 9c) to be at most  $4.28 \cdot 10^{-7}$  with a mean of  $\approx 1 \cdot 10^{-7}$ . The histogram Figure 9e confirms values of  $\Delta_1 > 1 \cdot 10^{-5}$  to be the exception (23 out of 500 data points). The median of  $\log_{10}(\Delta_1) - 6.02$  is close to the mean of  $-6.16$ .

The distribution of  $\Delta_2$  over  $\Xi_2$  in Figure 9b differs distinctly from the distribution of  $\Delta_1$  (Figure 9a). A band along the central wavelength is well resolved for all incidence angles. Similarly, at the boundaries the error is minimal. Overall, we observe  $\Delta_2$  to smaller than  $2.62 \cdot 10^{-8}$ . The relative error distribution in (Figure 9d) is almost identical, albeit with error levels four magnitudes smaller. The median and mean of  $\log_{10}(\Delta_2)$  in Figure 9f are  $\approx -12$ .

In Figures 9a-d the positions of the EIM snapshots for the matrix and right-hand sides are marked as blue diamonds and squares. Their locations coincide with minima of both  $\Delta_1$  and  $\Delta_2$ . Best observed in the relative errors  $\delta_1$  and  $\delta_2$  is the structure of the errors. Along the lines connecting the central snapshot and the snapshots on the boundaries in parameter space, the error is lowest. For the errors  $\Delta_1, \delta_2$  we observe an anisotropy in the error along the wavelengths of the snapshots employed for the matrices. This is of little surprise, as this error measures the deviations in the inverse of  $\mathcal{A}$  and  $\mathcal{A}_{eim}$  acting on  $\mathbf{b}_{eim}$ , as

$$\begin{aligned}\Delta_2 &= \|\tilde{\mathbf{x}} - \mathbf{x}_{eim}\|_{\mathbf{H}(\mathbf{curl}, \Omega)} = \|\mathcal{A}^{-1}\mathbf{b}_{eim} - \mathcal{A}_{eim}^{-1}\mathbf{b}_{eim}\|_{\mathbf{H}(\mathbf{curl}, \Omega)} \\ &= \|(\mathcal{A}^{-1} - \mathcal{A}_{eim}^{-1})\mathbf{b}_{eim}\|_{\mathbf{H}(\mathbf{curl}, \Omega)}.\end{aligned}$$

As in this study the incidence angle and wavelength have been varied, the parameter dependency of the matrices are not as pronounced as the right-hand side dependency. This can be observed here in the different magnitudes of the errors  $\Delta_1$  and  $\Delta_2$ .

We conclude that the relative errors introduced by the empirical interpolation approximation of the matrix and right-hand side are satisfyingly controlled. However, in the vicinity of the resonance band where the condition of the matrix is worse these errors might be substantial in absolute terms.

## 5. CONCLUSION

A reduced basis method based on the *hp*-finite element method for the electromagnetic scattering problem for general parameter dependencies has been presented. Construction, evaluation and accuracy of the reduced basis approximation have been discussed in detail for a photonic crystal structure made of silicon with a parameterized illumination source. The method allows to compute online solutions in milliseconds even in the presence of resonances. The accuracy of the approximation is reduced at the resonance positions and a lower empirical interpolation tolerance setting might improve the accuracy in future applications.

## ACKNOWLEDGMENTS

The results were obtained at the Berlin Joint Lab for Optical Simulations for Energy Research (BerOSE) of Helmholtz-Zentrum Berlin für Materialien und Energie, Zuse Institute Berlin and Freie Universität Berlin. Further we acknowledge support by the Einstein Foundation Berlin through ECMath within subprojects SE6 and OT5.

## REFERENCES

- [1] Monk, P., [*Finite Element Methods for Maxwell's Equations*], Numerical Mathematics and Scientific Computation, Clarendon Press (2003).
- [2] Maes, B., Petráček, J., Burger, S., Kwiecien, P., Luksch, J., and Richter, I., “Simulations of high-Q optical nanocavities with a gradual 1D bandgap,” *Optics Express* **21**, 6794 (Mar. 2013).
- [3] Pomplun, J., Burger, S., Zschiedrich, L., and Schmidt, F., “Reduced basis method for real-time inverse scatterometry,” *Proc. SPIE* **8083**, 808308 (2011).
- [4] Prudhomme, C., Rovas, D. V., Veroy, K., Machiels, L., Maday, Y., Patera, A. T., and Turinici, G., “Reliable Real-Time Solution of Parametrized Partial Differential Equations: Reduced-Basis Output Bound Methods,” *Journal of Fluids Engineering* **124**(1), 70 (2002).
- [5] Rozza, G., Huynh, D. B. P., and Patera, A. T., “Reduced Basis Approximation and a Posteriori Error Estimation for Affinely Parametrized Elliptic Coercive Partial Differential Equations,” *Archives of Computational Methods in Engineering* **15**, 229–275 (May 2008).
- [6] Pomplun, J., *Reduced basis method for electromagnetic scattering problems*, phdthesis, Free University Berlin (2010).
- [7] Eftang, J. L., Patera, A. T., and Rønquist, E. M., “An ”hp” Certified Reduced Basis Method for Parametrized Elliptic Partial Differential Equations,” *SIAM Journal on Scientific Computing* **32**, 3170–3200 (Jan. 2010).
- [8] Pomplun, J., Burger, S., Zschiedrich, L., and Schmidt, F., “Adaptive Finite Element Method for Simulation of Optical Nano Structures,” *Physica Status Solidi (B)* **244**, 3419–3434 (Oct. 2007).
- [9] Gschrey, M., Thoma, A., Schnauber, P., Seifried, M., Schmidt, R., Wohlfeil, B., Krüger, L., Schulze, J.-H., Heindel, T., Burger, S., Schmidt, F., Strittmatter, A., Rodt, S., and Reitzenstein, S., “Highly indistinguishable photons from deterministic quantum-dot microlenses utilizing three-dimensional in situ electron-beam lithography,” *Nature Communications* **6**, 7662 (2015).
- [10] Burger, S., Zschiedrich, L., Pomplun, J., Blome, M., and Schmidt, F., “Advanced finite-element methods for design and analysis of nano-optical structures: Applications,” *Proc. SPIE* **8642**, 864205 (2013).
- [11] Hammerschmidt, M., Lockau, D., Burger, S., Schmidt, F., Schwanke, C., Kirner, S., Calnan, S., Stannowski, B., and Rech, B., “FEM-based optical modeling of silicon thin-film tandem solar cells with randomly textured interfaces in 3D,” *Proc. SPIE* **8620**, 86201H (Mar. 2013).
- [12] Lockau, D., Sontheimer, T., Becker, C., Rudigier-Voigt, E., Schmidt, F., and Rech, B., “Nanophotonic light trapping in 3-dimensional thin-film silicon architectures,” *Opt. Express* **21**, A42–A52 (2013).
- [13] Wohlfeil, B., Burger, S., Stamatiadis, C., Pomplun, J., Schmidt, F., Zimmermann, L., and Petermann, K., “Numerical simulation of grating couplers for mode multiplexed systems,” *Proc. SPIE* **8988**, 89880K (Mar. 2014).
- [14] Zschiedrich, L., Blome, T., and Greiner, H. J., “Simulation of advanced OLED light extraction structures with novel FEM methods,” *SPIE Photonics Europe*, 91370O (2014).
- [15] Becker, C., Wyss, P., Eisenhauer, D., Probst, J., Preidel, V., Hammerschmidt, M., and Burger, S., “5 x 5 cm silicon photonic crystal slabs on glass and plastic foil exhibiting broadband absorption and high-intensity near-fields,” *Scientific reports* **4**, 5886 (Jan. 2014).
- [16] Demkowicz, L., Kurtz, J., Pardo, D., Paszenski, M., Rachowicz, W., and Zdunek, A., [*Computing with hp-ADAPTIVE FINITE ELEMENTS: Volume II Frontiers: Three Dimensional Elliptic and Maxwell Problems with Applications*], Chapman & Hall/CRC Applied Mathematics & Nonlinear Science, CRC Press (2007).
- [17] Burger, S., Zschiedrich, L., Pomplun, J., Herrmann, S., and Schmidt, F., “Hp-finite element method for simulating light scattering from complex 3D structures,” *Proc. SPIE* **9424**, 94240Z (Mar. 2015).

- [18] Pomplun, J. and Schmidt, F., “Accelerated a posteriori error estimation for the reduced basis method with application to 3D electromagnetic scattering problems,” *SIAM J. Sci. Comput.* **32**, 498–520 (2010).
- [19] Schmidt, F., Pomplun, J., Zschiedrich, L., and Burger, S., “Fast online simulation of 3D nanophotonic structures by the reduced basis method,” *Proc. SPIE* **7941**, 79410G–79410G–6 (Feb. 2011).
- [20] Barrault, M., Maday, Y., Nguyen, N. C., and Patera, A. T., “An empirical interpolation method: application to efficient reduced-basis discretization of partial differential equations,” *Comptes Rendus Mathématique* **339**, 667–672 (Nov. 2004).
- [21] Maday, Y., Nguyen, N.-C. N., Patera, A. T., and Pau, G., “A general, multipurpose interpolation procedure: the magic points,” *Communications on Pure and Applied Analysis* **8**(1), 383–404 (2007).
- [22] Quarteroni, A. and Rozza, G., “Numerical solution of parametrized Navier-Stokes equations by reduced basis methods,” *Numerical Methods for Partial Differential Equations* **23**, 923–948 (2007).
- [23] Eftang, J. L., Grepl, M. A., Patera, A. T., and Rønquist, E. M., “Approximation of Parametric Derivatives by the Empirical Interpolation Method,” *Foundations of Computational Mathematics* **13**, 763–787 (June 2012).
- [24] Joannopoulos, J. D., Johnson, S. G., Winn, J. N., and Meade, R. D., [*Photonic Crystals: Molding the Flow of Light (Second Edition)*], Princeton University Press (2011).
- [25] Palik, E. D., [*Handbook of Optical Constants of Solids*], no. Bd. 3 in Academic Press handbook series, Academic Press (1998).